5
Fabrication of Nickel Cobaltite Nanoplates for OER

(Cited work: Urgunde et al., Materials Research Bulletin 2021, 142, 111380)

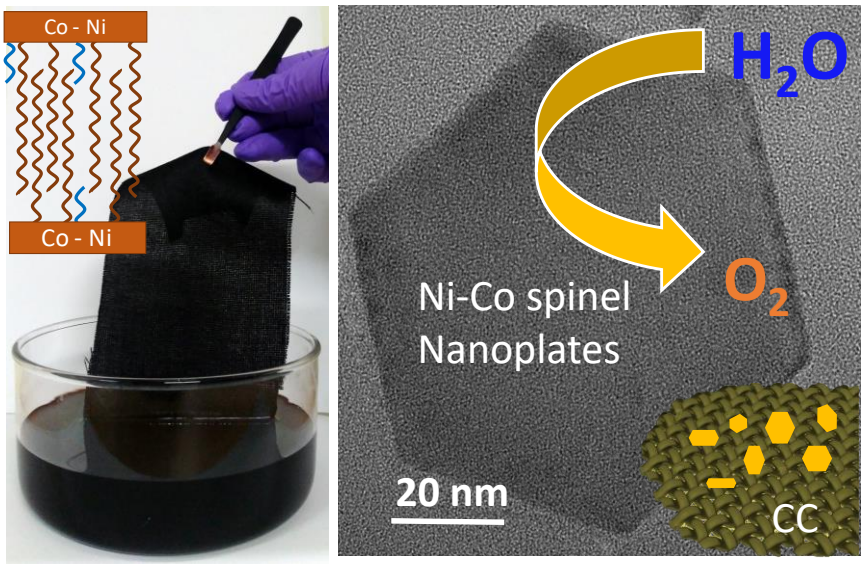

5.1 Introduction

Two dimensional nanostructures of $NiCo_2O_4$ have gained importance owing to its physical properties and phenomenal enhancement in electrocatalytic properties.[Hu et al., 2012] Electrodeposition technique and hydrothermal synthesis are commonly employed for the hierarchical growth of $NiCo_2O_4$ nanostructures on conducting substrates for carrying the OER process.[Silva et al., 2012; Yuan et al., 2012; Zhang et al., 2016c] However, all these techniques suffer from significant issues in terms of optimization of reaction conditions, experimental setup, and equipment capabilities, specifically when it comes to scalable synthesis.[Zeng et al., 2020] Further, the electrocatalysts grown by these methods require polymeric binders and conductive additives that add to the internal resistance in the electrode system.[Anantharaj et al., 2016; Urgunde et al., 2019] Hence, a scalable approach is necessary for mass production by overcoming the problems discussed above while maintaining the lower overpotential. A solution processing method can enable the manufacturing of electrodes with the flexibility of tuning the material composition for best performance. In this context, we use metal alkanethiolate precursor based inks dissolved in non-polar solvents with the film-forming ability for direct coating on 3D substrates with sufficiently low decomposition temperature for formation of the desired product.[Busupalli et al., 2016; Gupta et al., 2017a] The molecular inks are amenable for printing as well as patterning by various techniques such as soft lithography, micro-molding, inkjet printing, dip-pen, and nano-imprint lithography.[Bhuvana et al., 2010; John et al., 2007a; Lim et al., 2013; Veselska et al., 2019] Various metal alkanethiolates of Pd,[Bhuvana et al., 2010] Ag,[De La Rama et al., 2013] Cu,[Bryks et al., 2016], Ni[Urgunde et al., 2020] and Au[Badia et al., 1997] have been studied for the synthesis of metals, metal oxides, and sulfides since these give rise to the desired product with excellent control over composition and morphology. Metal alkanethiolates in solution phase, self-assemble into lamellar bi-layer structures.[Smith et al., 2019] The solubility of metal thiolates in non-polar solvents depends on the molecular structure and dynamics of the alkane chains.[John et al., 2007b] The alkane chain component of the metal-organic precursor, balances the strong intermolecular forces and

hydrophobic interactions resulting in an ordered supramolecular assembly. Interestingly, the shape of nanostructures formed by solventless thermolysis is known to depend on the lamellar, micellar, or isotropic phase adopted by the metal-organic precursors. For example, Tao *et al.* reported disk-shaped nanocrystals from the micellar phase and 2D thin sheets of $Cu_{2-x}S$ from ordered liquid crystalline mesophase of Cu thiolate precursors.[Binnemans et al., 2021; Bryks et al., 2014] In this work, the nickel butanethiolate (Ni-BT) and Co Hexadecanethiolate (Co-HDT) were chosen as inks to form mixed lamellar bilayer assemblies that give rise to interesting bimetallic Ni-Co spinel nanoplates by solventless decomposition method. Ni-alkanethiolate with square planar structure forms lamellar bilayer assembly and thus of interest as an easy coat ink with capability to form thin films and printed patterns for the fabrication of Ni nanostructures.[Rao et al., 2011b] As per our knowledge, there are no reports related to the supramolecular organization of mixed metal thiolates for bimetallic spinel formation. Electrocatalyst, NCO-20 formed by this method, exhibits excellent electrocatalytic activity towards oxygen evolution reaction (OER) for water oxidation, and is studied by XPS measurements. The influence of magnetic field on OER performance of superparamagnetic 2D nanoplates of NCO is further explored in this study.

5.2 Objectives of the Work

The objectives of this work are as follows:

1. To study the effect of mixed metal alkanethiolates on anisotropic lamellar assembly formation.
2. To synthesize spinel type Ni-Co oxides using mixed Ni-BT and Co-HDT inks.
3. To optimize the electrochemical performance of Ni-Co spinel oxides towards OER.
4. To study the magnetic properties of $NiCo_2O_4$ nanostructures and magnetic field-assisted OER.

5.3 Experimental

5.3.1 Characterization

Thermogravimetric analysis (TGA) of metal alkanethiolate complexes (10 mg) was performed at a rate of 10 °C/min by using a Simultaneous Thermal Analyzer, Perkin Elmer equipped with a digital temperature controller from Poly Science. CHNS analysis was carried out using Elemental Vario EL III. The compositional CHNS analysis of Ni-BT and Co-HDT confirms the formation of $M(SR)_2$ complex, where R is an alkane chain. The mass loading is calculated from the mass difference of the bare carbon cloth and the thermolysed carbon cloth after dip-coating through TGA analysis. X-ray diffraction (XRD) patterns were recorded from 20° to 70° at a scan rate of 0.05°/s using Bruker D8 Advance with Cu Kα (λ=1.540 Å). Raman spectra were acquired with Renishaw, UK, using a diode laser with a wavelength of 523 nm. Magnetic measurements were performed using the Dynacool physical properties measurement system (PPMS) from Quantum Design. Magnetic hysteresis (M-H) loops were obtained at 300 K in the field range of ±50 kOe. Morphology was examined byfield–emission scanning electron microscopy (FESEM) (Nova NanoSEM 600 instrument, FEI Co., The Netherlands). HRTEM and ED patterns were recorded using Talos 2000S G2 FEG with a beam energy of 200 kV, and *d*-spacings were calculated using Gatan Microscopy Suite (GSM). X-ray photoelectron spectroscopy (XPS) was carried out using Omicron Nanotechnology (Oxford Instruments) on the electrodes prepared by 25 consecutive CV cycles in a voltage range of 1.0 to 1.6 V versus RHE in 1 M KOH for surface activation and stable response.

5.3.2 Electrochemical Characterization of the Electrocatalyst

Conducting CC was purchased from Fuel Cell Earth LLC (Product Code CP40). The NCO-based electrodes were directly prepared by dip-coating CC substrate of 0.5 cm^2 in Ni-Co thiolates (5 mg/mL) with different molar ratios, following which it was thermolysed at 350°C in a nitrogen atmosphere for 3 hrs. The coating conditions were kept constant during all depositions for the sake of comparison of results. The electrochemical properties were studied on the electrochemical workstation (CHI 660E) in a three-electrode geometry containing an Ag/AgCl reference electrode and Pt as a counter electrode. The measurements were carried out in a solution of 1 M KOH (pH = 14). The NCO/CC were used as the working electrode for the electrochemical measurements. Before electrochemical measurements, the electrodes were activated by carrying out 25 consecutive CV scans in 1 M KOH and a voltage range of 1 to 1.6 V versus RHE till a stable overlapping response was obtained. The linear sweep voltammetery (LSV) was recorded in the voltage range of 0 to 0.6 V versus Ag/AgCl electrode and expressed as reversible hydrogen electrode (RHE) using the given in setion 2.6 of chapter 2. Cyclic Voltammetry (CV) was carried out in the non-faradic region (1.22 V to 1.25 V versus RHE) at different scan rates for calculation of electric double-layer capacitance (C_{dl}). Electrochemical impedance spectroscopy (EIS) measurements were performed using an in-built impedance module of the workstation. Data were collected at 0.62 V versus Ag/AgCl in a frequency range from 0.1 Hz to 10 MHz and the potential amplitude of 10 mV. For magnetic experiments, the electrochemical setup for OER measurements was placed in an applied magnetic field of 300 mT.

5.4 Results and Discussion

5.4.1 Synthesis of Co Hexadecanethiolate and Ni butanethiolate Precursors

The Co-HDT and Ni-BT precursors were synthesized using general two step process, detailed in Chapter 2, section 2.4.2.

5.4.2 Characterization of Mixed Ni-BT and Co-HDT Inks

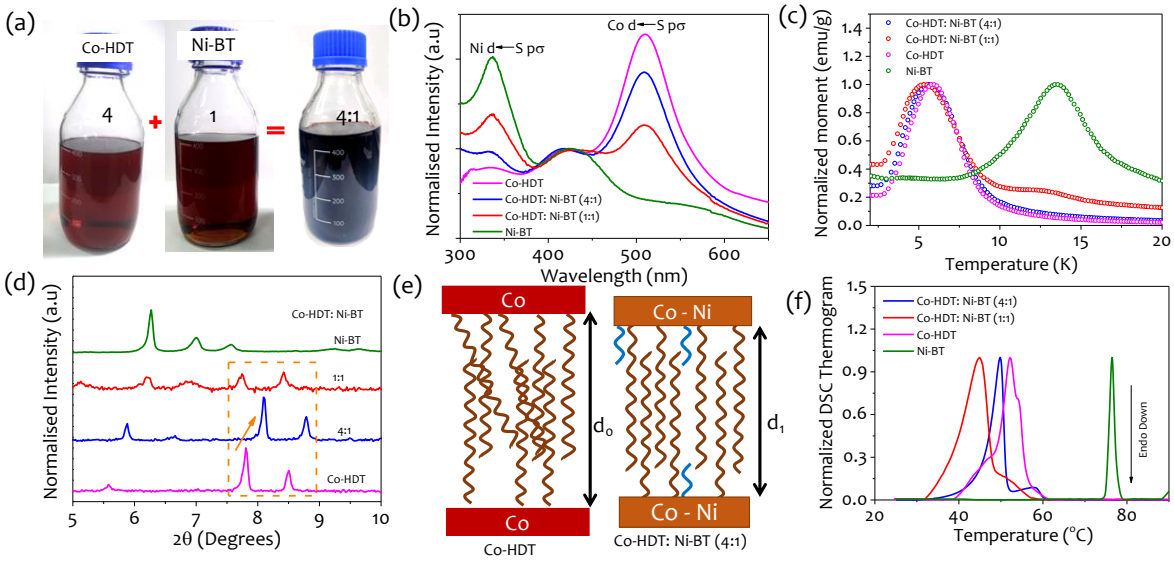

Figure 5.1: (a) Digital photographs of Ni-BT, Co-HDT and corresponding mixture ink (b) UV-visible spectra, (c) M-T (ZFC) curves and (d) XRD patterns, (e) Schematic representing the lamellar structure of Co-HDT compared with Co-HDT:Ni-BT (4:1) and (f) DSC thermograms.

The Ni butanethiolate (Ni-BT) and Co Hexadecanethiolate (Co-HDT) complexes were synthesized in gram scale and mixed in 4:1 molar ratio. For scalable synthesis, 500 mL of Ni-Co based thiolate ink formulation was prepared by dissolving 2.26 g of Co-HDT complex and 0.23 g of the Ni-BT complex together in toluene as depicted in Figure 5.1a. Ni thiolate complex with short butane chain and Co thiolate complex with long hexadecane chain exhibited maximum solubility in toluene and thus, chosen for this study. Ni-BT is blackish-brown, and Co-HDT has a deep red color due to ligand to metal (S→Ni, Co) charge transfer bands, respectively (Figure 5.1b). A mixture of Co-HDT: Ni-BT in 4:1 and 1:1 ratios exhibit similar spectrum to that of single components without any peak shift. Upon addition of Ni-BT to Co-HDT, the absorption at 510 nm was gradually decreased, and the intensity of the band at 336 nm increased, as expected (Figure 5.1b).[John et al., 2007b] Magnetic moment versus temperature, zero-field cooled (ZFC), and field cooled (FC) were performed in the range of 2 -300 K at an applied field of 100 Oe. Usually, an increase in magnetization is observed at lower temperatures with further splitting of ZFC and FC at a critical transition temperature (T_C). ZFC curves shown in Figure 5.1c are normalized for clarity. Ni-BT exhibits a T_C at 13.6 K, which is in conjugation with the reported value.[John et al., 2007b] For Co-HDT, T_C is observed at 5.9 K.

Figure 5.2: Photograph of carbon cloth coated with Ni-Co ink (35 × 10 cm^2) demonstrating scalability of the synthesis process.

The lower T_C for Co-HDT can be related to the steric hindrance of the long-chain, which restrain from going to the antiferromagnetic arrangement. Interestingly, in the case of 4:1, a slight shift in T_C with respect to Co-HDT is observed, possibly due to magnetic exchange interactions between Co and Ni at a molecular level. Further, the magnetic moment contributions in the mixture are highly dominated by Co-HDT even in the case of 1:1 mixture due to the intrinsic magnetic moment of Co^{2+} (paramagnetic) in comparison to that of Ni^{2+} (diamagnetic). XRD patterns for both Ni-BT and Co-HDT (Figure 5.1d) show sharp peaks that correspond to a crystalline structure. Ni-BT, being square planar, possesses a lamellar bi-layer structure where the d-spacing is calculated to be 14.17 Å that matches with the theoretically calculated value based on the molecular model.[John et al., 2003] On the contrary, the Co-HDT pattern could not be matched with the molecular structure, probably due to interdigitation and entanglement of the alkane chains. Interestingly, the addition of Ni-BT to Co-HDT has a remarkable effect on the interplanar spacing of alkane chains in Co-HDT. There is a significant shift in peaks of 4:1 mixture to higher 2θ values. This could be attributed to an increase in the interdigitation of long C16 alkane chains due to the accommodation of C4 chains, thus reducing the d-spacing by 0.830 Å (d_0-d_1) as depicted schematically in Figure 5.1e. However, a 1:1 mixture of Co-HDT and Ni-BT resulted in the distortion of Co-HDT structure with a decrease in intensity of ordered peaks (highlighted in Figure 5.1d) without any shift and change in interplanar spacing. DSC curves in Figure 5.1f show a broad peak for endothermic heat flow at 52.2 °C for Co-HDT and a sharp peak at 76.4°C for Ni-BT, which are expected due to the differences in chain length and structural properties.[Smith et al., 2019]

5.4.3 Characterization and Fabrication of Ni-Co Oxides based Electrodes

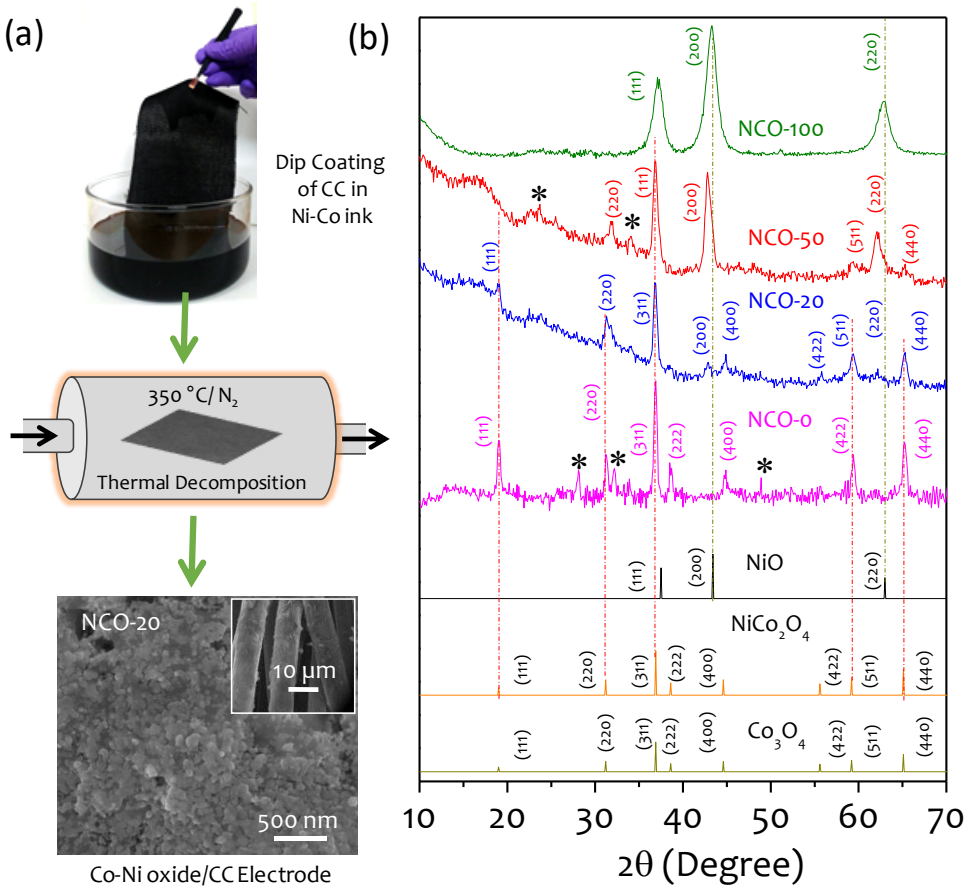

Figure 5.3: (a) Photograph of carbon cloth (35 x 10 cm^2) dip-coated in Ni-Co ink with schematic demonstrating the process steps involved in the overall fabrication of NCO on carbon cloth for OER. (b) XRD patterns of Ni-Co oxides are abbreviated as NCO-0, NCO-20, NCO-50, and NCO-100 based on Ni%. (Note * denotes non-indexable planes)

Interestingly, the endothermic peak due to phase transition gets sharp and narrower for Co-HDT: Ni-BT (4:1) bilayer assembly with slight temperature shift indicative of long-range ordering. In the case of 1:1 mixture, an excess of Ni-BT molecules interfere in the packing and confinement of C16 alkane chains that lead to a decrease in the cooperativity of the phase transition resulting in broadening of peak. Thus, 4:1 assembly of Co-HDT: Ni-BT resulted in a mesogenic organization that was further used to synthesize Ni-Co oxide (NCO) nanostructures. Figure 5.3a describes the experimental procedure involved in the fabrication of Ni-Co oxides (NCO) over carbon cloth (CC). Ni-Co ink is dip-coated on carbon cloth substrate (35 × 10 cm^2) and thermolysed to give NCO coating as shown in Figure 5.2. Given the simplicity of the dip coating and thermolysis process, the technique adopted in this work is industrially scalable compared to other synthetic methods such as hydrothermal, electrodeposition, and CVD. Briefly, carbon cloth (CC) substrates are dip coated in different ratios of Co:Ni inks and thermolysed at 350 °C in the nitrogen environment to form NCO as an electrocatalyst of desired composition (Figure 5.3a). From TGA curves (Figure 5.4), a temperature of 350 °C was chosen for thermolysis. These electrocatalysts supported on CC were labeled as NCO-x/CC, where x corresponds to Ni%. The FESEM image of NCO-20/CC shows uniformly and densely coated CC fiber with NCO nanostructures. The coating conditions were kept constant to obtain a uniform thiolate ink loading of ~1.1 mg/cm^2.

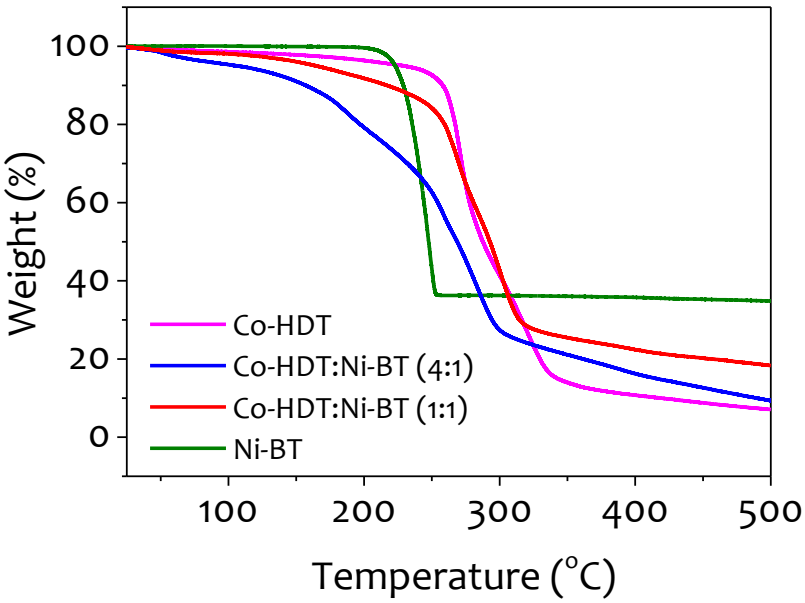

Figure 5.4: Thermogravimetric Analysis (TGA) of Co-HDT:Ni-BT of Co-HDT, 1:1, 4:1 and Ni-BT at 10 °C/min in N_2.

The crystal structure and phases of NCO formed were analyzed using XRD, qualitatively (Figure 5.3b). The XRD pattern of cobalt oxide (NCO-0) matches precisely with the polycrystalline cubic spinel structure of Co_3O_4, and nickel oxide (NCO-100) exhibits planes corresponding to face-centered cubic NiO without any impurity peak. The XRD pattern of NCO-20 shows the presence of the $NiCo_2O_4$ spinel with predominant 311 orientations, while NCO-50 resulted in the formation of a mixture of NiO and spinel phase.

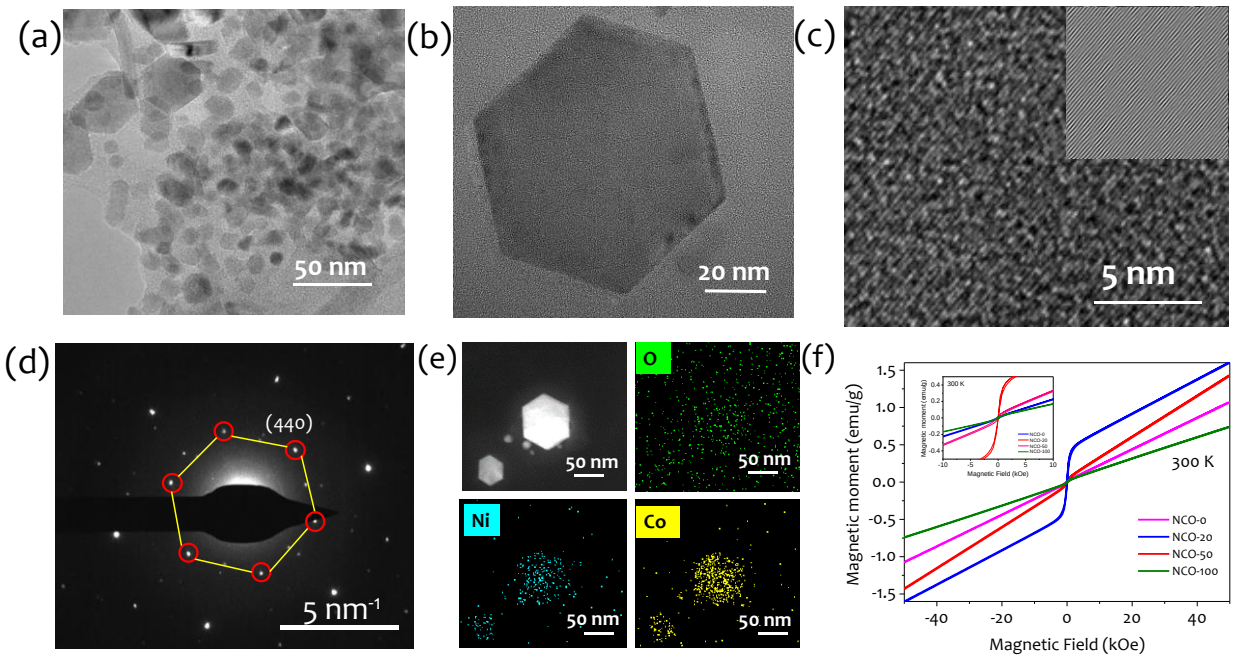

Figure 5.5: (a-b) Transmission Electron Micrograph (TEM) images of NCO-20 nanoplates (c) HRTEM image showing 422 planes (d-spacing ~1.65 Å) obtained from a magnified area of the nanoplate. Inset shows corresponding i-FFT analysis. (d) SAED pattern. (e) EDS mapping (f) M-H curves at 300 K. Inset in f shows the magnified region.

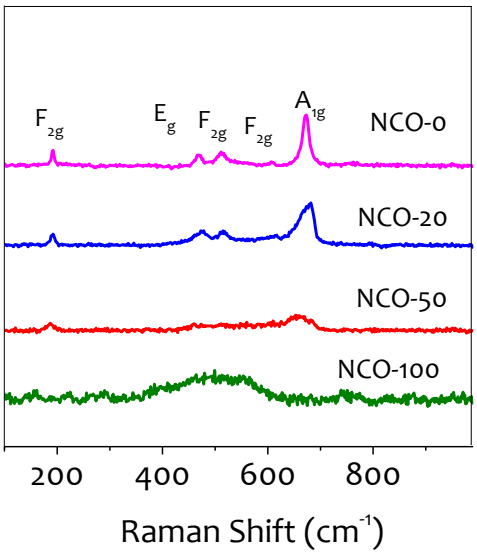

Figure 5.6: Raman spectra of NCO-0, NCO-20, NCO-50, and NCO-100.

Raman spectra corroborate well with the structural changes observed in the XRD patterns (Figure 5.6). Raman spectrum of NCO-20 exhibits a blue-shifted A_{1g} peak due to the incorporation of Ni in the octahedral site resulting in $NiCo_2O_4$ formation.[Iliev et al., 2013] The NCO-20 is further characterized using HRTEM images to examine the morphology in detail (Figure 5.5). Interestingly, thin polygonal nanoplate-type structures of ~5-30 nm size are seen embedded in the carbon matrix formed during the thermolysis of Co-Ni (4:1) precursor film (Figure 5.5a). The conducting carbon matrix left out from the precursor's decomposition serves as an adhesive for the nanostructures on the CC substrate. A magnified view of one of the hexagonal nanoplates is shown in Figure 5.5b. Overall, the size, lateral thickness, and shape of nanoplates vary due to the differences in the extent of ordering in the self-assembled thiolate complex before thermolysis. The nanoplates are formed by the stacking of atomically thin nanosheets by Van der Waal interactions between them. The formation of nanoplates is indeed interesting.

In mixed thiolate precursor (Co-HDT:Ni-BT of 4:1), the ordering in bilayer assembly of molecules was evident from the sharpness in DSC profile, higher magnetic exchange interaction, and lower interlayer spacing in XRD pattern (Figure 5.1). The 4:1 mixed precursor forms anisotropic assembly of Ni-Co in the form of a bilayer structure, and the atomically thin Ni-Co slab shown in Figure 5.1e defines the thickness of the low dimensional nanostructures of $NiCo_2O_4$. The non-uniformity in nanoplates can arise from the defects in bilayer assembly from unbound thiol molecules, and tuning various other parameters such as annealing time and molar concentration may result in uniform size distribution. In literature, such anisotropic structures of CuS in the form of nanosheets were obtained from lamellar assembly of short chain Cu alkanethiolates.[Bryks et al., 2016; Du et al., 2007; Larsen et al., 2003] The HRTEM image of an isolated hexagonal nanoplate show well-resolved lattice fringes of 1.65 Å corresponding to 422 planes of spinel structure (Figure 5.5b and c). The thin nanoplates are observed to be oriented along different crystallographic planes of 220, 311, and 422 corresponding to spinel structure (see detailed analysis in Figure 5.7). The SAED pattern shows hexagonally arranged sharp diffraction spots corresponding to single-crystalline nature (Figure 5.5d).[Hu et al., 2011] The elemental mapping of the sample with 20% Ni in Figure 5.5e reveals that Ni and Co are homogeneously distributed across the surface, indicating the formation of a solid solution resulting in $NiCo_2O_4$ type spinel.

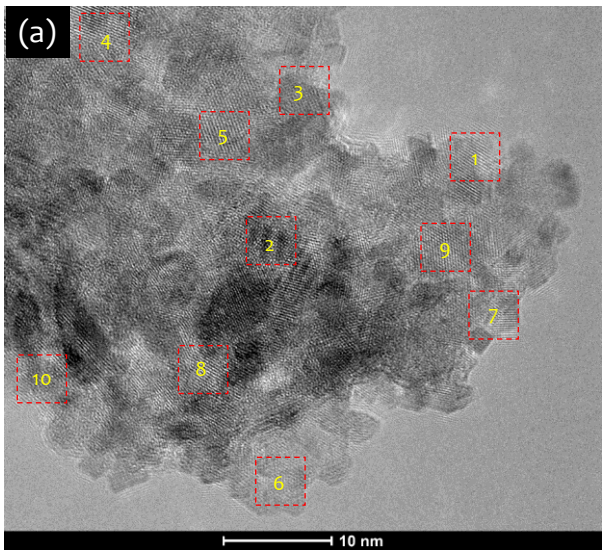

Area	d (Å)	Spinel
1	2.4444	311
2	2.8731	220
3	2.8731	220
4	1.6518	422
5	2.4444	311
6	2.8731	220
7	1.6518	422
8	2.4444	311
9	2.4444	311
10	2.8731	220

Figure 5.7: HRTEM image of NCO-20 nanoplates and its analysis alongside from 10 different areas.

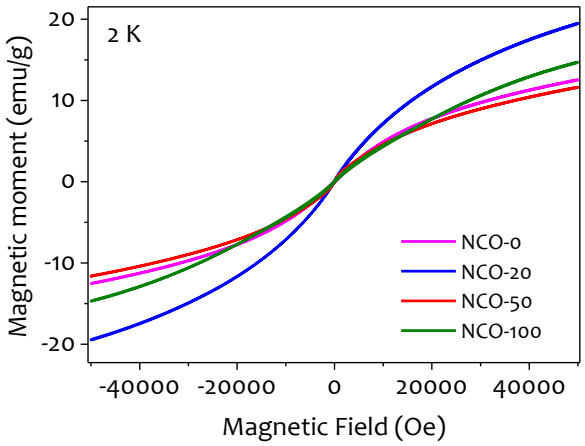

Figure 5.8: M-H curves of NCO-0, NCO-20, NCO-50 and NCO-100 at 2 K.

The M-H curve at low temperature (2 K) is shown Figure 5.8. M-H curve at room temperature (300 K) of NCO-20 shows superparamagnetic behavior due to thin plate-type $NiCo_2O_4$ (Figure 5.5f).[Verma et al., 2008, 2014] Contrastingly, the pristine Co_3O_4, NiO, and NCO-50 exhibit linear M-H curves indicating AFM behavior at room temperature. A kink observed in the AFM response at low magnetic fields in NCO-50 originate from the superparamagnetic contribution of spinel present along with the majority of NiO and Co_3O_4.

5.4.3 Electrochemical Performance towards OER

To further study the electrocatalytic activity towards OER, electrodes were characterized using various electrochemical techniques in three-electrode geometry with 1 M KOH. The electrodes were prepared by 25 consecutive CV cycles in a voltage range of 1.0 to 1.6 V versus RHE in 1 M KOH for surface activation and stable response (Figure 5.9). LSV measurements of all NCO electrodes were performed, as shown in Figure 5.10a. Interestingly, NCO-20/CC with spinel phase dominates significantly over pristine oxides, current density @1.65 V, onset potential (260 mV), and overpotential (310 mV for J = 10 mA/cm^2) for electrodes prepared under the same conditions. The onset potential and overpotential values (@10 mA/cm^2 and 100 mA/cm^2) towards OER as tabulated in Table 5.2. The overpotential of the fabricated electrodes compares favorably with those of the documented Co and Ni-based electrocatalysts reported in the literature (Table 1.3).

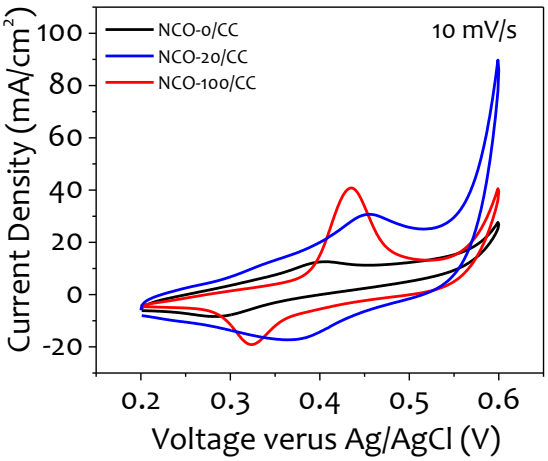

Figure 5.9: (a) CV curves of pristine Co_3O_4 (NCO-0/CC), NiO (NCO-100/CC) and NCO-20/CC at 10 mV/s in 1 M KOH.

The kinetics of the OER for NCO-20/CC was examined by Tafel plot. Tafel plot was derived from the LSV recorded at 5 mV/s and linearly fitted to evaluate the efficacy of NCO-20 as electrocatalyst (Figure 5.10b).[Chang et al., 2018] The Tafel slope for NCO-20 is lowest (68.4 mV/dec), which is attributed to the increase in kinetic activity of the nanoplates' surface-active catalytic sites.

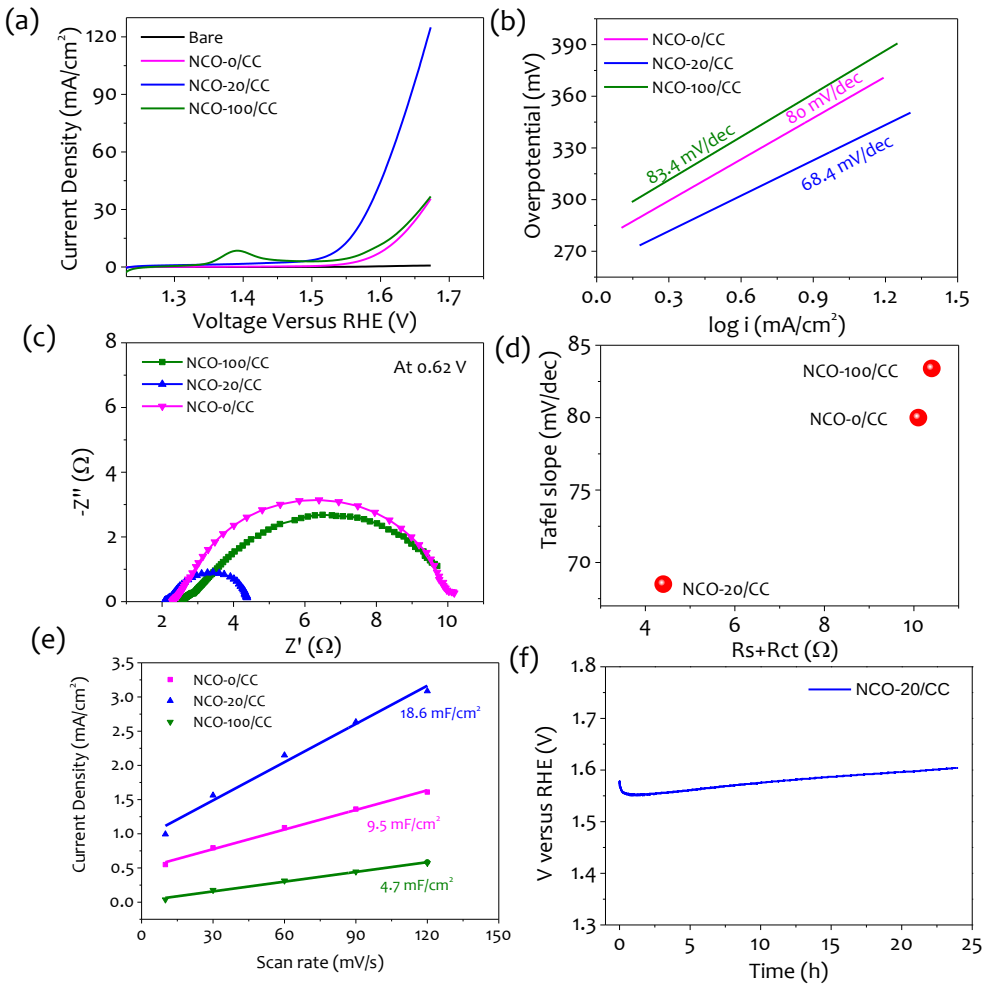

Figure 5.10: (a) LSV curves at 5 mV/s, (b) Tafel plot, (c) Nyquist plot (d) Tafel slope versus total resistances, and (e) current density versus scan rate for C_{dl} calculation of NCO-0/CC, NCO-20/CC, and NCO-100/CC. (f) Chronopotentiometry at 10 mA/cm² of NCO-20/CC.

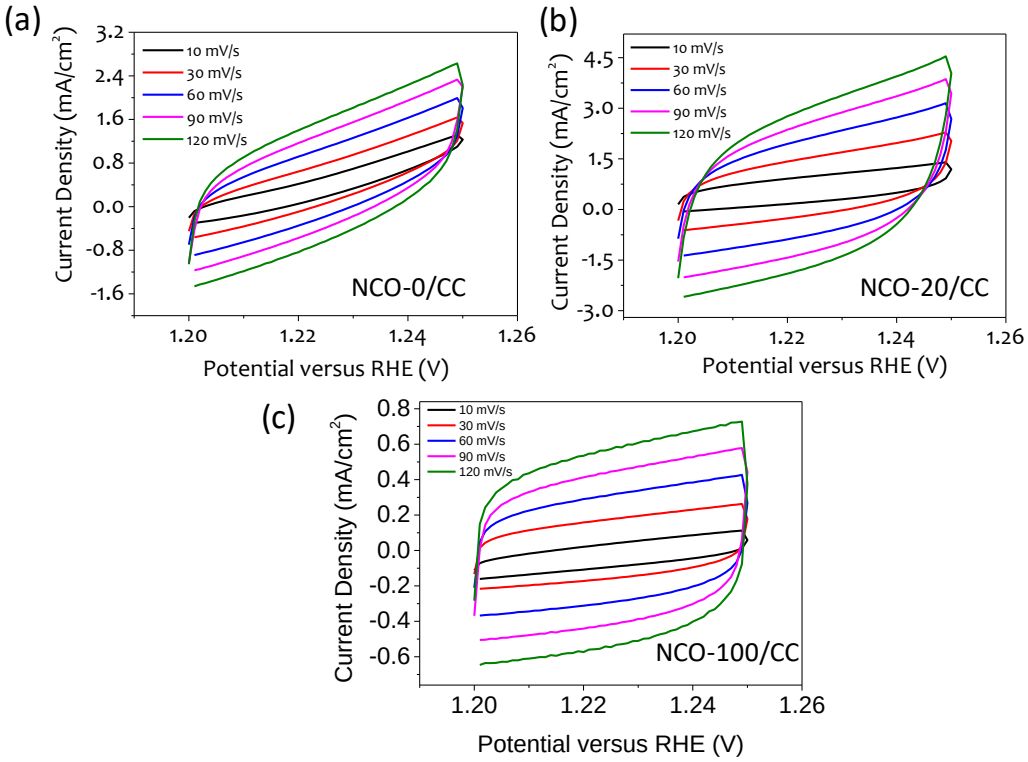

Figure 5.11: CV of Co-Ni oxides on carbon cloth (CC) with (a) NCO-0/CC, (b) NCO-20/CC (c) NCO-100/CC at different scan rates ranging between 10-120 mV/s.

EIS was carried out to investigate the system's resistances and understand the OER reaction kinetics (Figure 5.10c) (for details, see experimental section). The net resistances are obtained as a sum of electrolytic resistance (R_s) and charge transfer resistance (R_{ct}). In case of NCO-20, the lower resistance ~ 4.4 Ω indicates faster OER. The plot of the Tafel slope versus total R_s+R_{ct} is shown in Figure 5.10d. The lower Tafel slope and resistance in NCO-20/CC followed by pristine oxides indicate the enhanced kinetic activity with lower resistance leading to higher OER performance. The NCO-20/CC electrode exhibits TOF of 3.9 $\times 10^{-2}$ s^{-1} (for calculations, see section 2.6 of chapter 2), which is comparable to the literature values. The C_{dl} of NCO-20/CC, along with the pristine oxides, was examined to understand the difference in the contributions of the active surface area responsible for OER activity. The C_{dl} of NCO-20/CC was significantly higher than the pristine oxides, as seen in Figure 5.10e (Figure 5.11). Overall, NCO-20/CC shows high kinetically active reaction sites for enhanced OER. The stability test for NCO-20/CC was carried out over 24 h by chronopotentiometry measurements at a current density of 10 mA/cm² (Figure 5.10f). No significant loss of catalyst was observed during OER, indicating the firm adhesion of electrocatalyst on CC. The superior performance and long term stability of NCO-20/CC can be attributed to the crystalline $NiCo_2O_4$ spinel phase present in the system.[Hu et al., 1997] Spinels provide faster ion transport and charge transfer because of its multiple oxidation states compared to pristine metal oxides.[Natarajan et al., 2017] For understanding the excellent performance of NCO-20 content-based NCO, further characterization of electrocatalyst is indispensable. The surface states of NCO based electrocatalysts responsible for high OER catalytic activity were investigated by XPS. The electrode surface was activated by 25 consecutive CV cycles in a voltage range of 1.0 to 1.6 V versus RHE in 1 M KOH. The high-resolution Ni 2p, Co 2p, and O 1s spectra of NCO-20/CC along with pristine NiO and CO_3O_4 are shown in Figure 5.12 The binding energy values assigned after the deconvolution of the respective signals of Co 2p, Ni 2p, and O1s are tabulated in Table 5.2.

Table 5.1: Calculated values of onset potential, overpotential, Tafel slope, and net resistances.

S.No	Electrode	Onset potential (mV)	Overpotential (mV) @ 10 mA/cm^2	Overpotential (mV) @ 100 mA/cm^2	Tafel slope (mV/dec)	R_s+R_{ct} (Ω)
1	NCO-0/CC	310	380	550	80	10.1
2	NCO-20/CC	260	310	420	68.5	4.4
3	NCO-100/CC	300	360	530	83.4	10.4

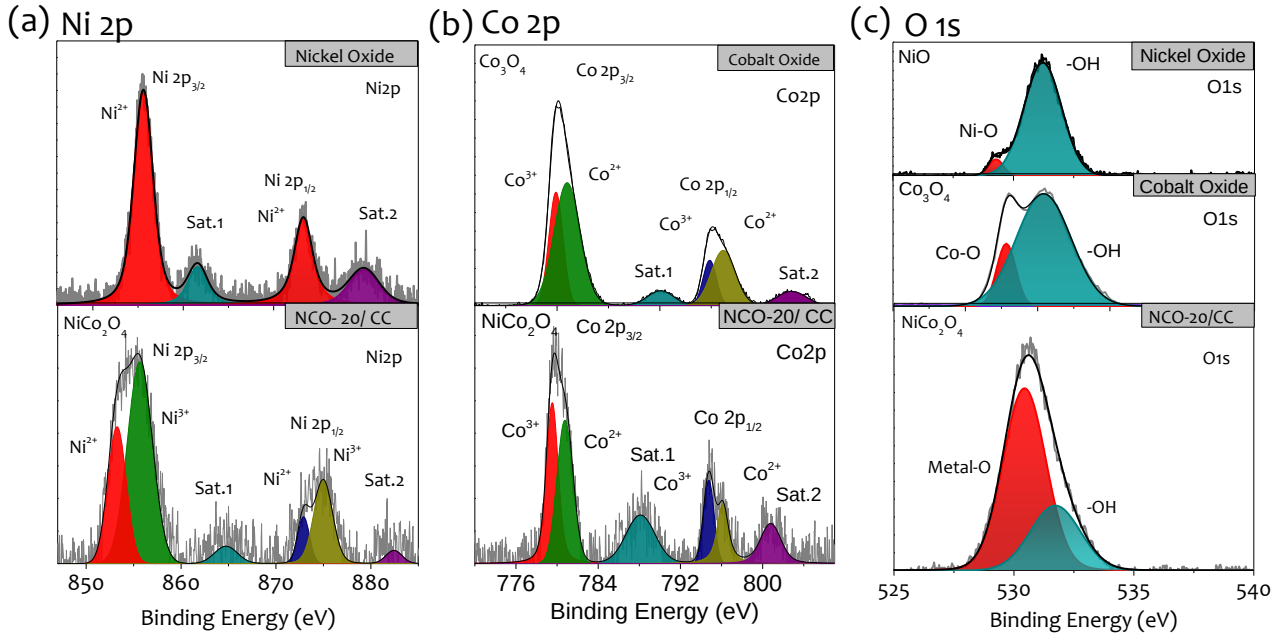

Figure 5.12: High-resolution X-ray Photoelectron Spectroscopy (XPS) spectra of NCO-0/CC (Co_3O_4), NCO-20/CC, and NCO-100/CC (NiO) after activation of electrodes by CV cycling. (a) Ni 2p (b) Co 2p and (c) O 1s core-level spectra.

Table 5.2: Binding Energy (BE) values derived from deconvoluted XPS spectra of Co 2p, Ni 2p, and O 1s.

S.No	Ni (eV)						Co (eV)						O (eV)		
NCO	Ni^{3+}		Ni^{2+}		Sat-1	Sat-2	Co^{3+}		Co^{2+}		Sat-1	Sat-2	Hydroxyl	Ni-O	Co-O
	$2p_{3/2}$	$2p_{1/2}$	2 $p_{3/2}$	$2p_{1/2}$	$2p_{3/2}$	2 $p_{1/2}$	2 $p_{3/2}$	2 $p_{1/2}$	2 $p_{3/2}$	2 $p_{1/2}$	2 $p_{3/2}$	2 $p_{1/2}$	N.A.	N.A.	N.A.
0	N.A.	N.A.	855.5	873.2	861.4	880	N.A.	N.A.	N.A.	N.A.	N.A.	N.A.	531.3	529.7	N.A.
20	855.6	874.9	853.2	872.9	864.8	882.2	779.5	794.8	780.9	796.1	788.0	800.7	531.7	530.4	
100	N.A.	N.A.	N.A.	N.A.	N.A.	N.A.	779.9	794.8	781	796.1	790.2	802.7	531.2	N.A.	529.1

Note: N.A indicates that the values are not available.

As seen in high-resolution Ni 2p XPS spectra (Figure 5.12 a) of NCO-0/CC, the presence of Ni^{2+} confirms the formation of NiO. The absence of Ni^{3+} species can be explained on the basis of the CV activation cycles during which the oxidized Ni species reduces back to Ni^{2+} and does not appear in XPS of pristine NiO. NCO-20/CC exhibits significant differences in the Ni 2p spectrum in comparison to that of pristine NiO. In NCO-20/CC, Ni $2p_{3/2}$ and Ni $2p_{1/2}$ peaks are deconvoluted to the Ni^{2+} and Ni^{3+} species where Ni^{3+} is attributed to the formation of $NiCo_2O_4$

spinel.[Xue et al., 2019] Moreover, an increase in Ni^{3+} species at the expense of Ni^{2+} also correspond to surface oxidation of Ni species that enhance the overall OER activity.[Gao et al., 2017]

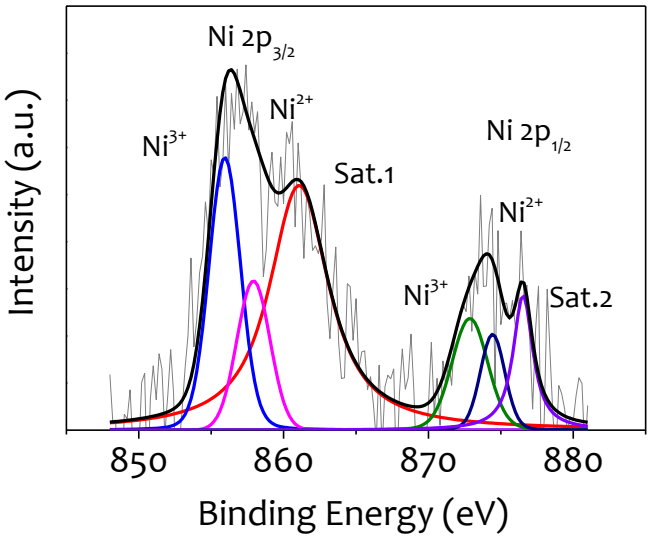

Figure 5.13: Deconvoluted Ni 2p spectra of pristine NCO-20/CC electrode before CV cycling.

As calculated from XPS analysis, Ni^{3+}/Ni^{2+} ratio is 2 in NCO-20/CC which is ~4 times higher than as prepared electrode (0.55, Figure 5.13). Hence, an increase in Ni^{3+} at the NCO-20/CC surface can be related to the enhanced surface oxidation of the $NiCo_2O_4$ spinel nanoplates. Figure 5.12b shows the high-resolution deconvoluted Co 2p spectra of NCO-20/CC and pristine Co_3O_4 for comparison as a control. The difference in the ratio of Co^{2+}/Co^{3+} in NCO-20/CC with respect to that of the pristine Co_3O_4 is also an indicator of $NiCo_2O_4$ formation. The lower the ratio of Co^{2+}/Co^{3+}, the more beneficial it is for OER. Higher Co^{3+} allows more OH^- adsorption leading to Co^{3+}/Co^{4+} species at an accelerated rate.[Yang et al., 2018b]

Table 5.3: XPS peak ratio analysis of Ni 2p, Co 2p, and O 1s spectra of NCO-based electrocatalysts.

S.No	Electrode	Co^{2+}/Co^{3+}	Ni^{3+}/Ni^{2+}	–OH/O l s
1	Co_3O_4/CC	2.02	N.A	0.82
2	NCO-20	1.07	2.00	0.71
3	NiO/CC	N.A	N.A	0.75

Note: N.A indicates that the values are not applicable

Mechanistically, Co^{4+} facilitates the formation of O−OH intermediates, accelerating the deprotonation of −OOH species to generate oxygen via the electron-withdrawing inductive effect.[Yang et al., 2014; Yeo et al., 2011b] Moreover, the intensity of the satellite Co 2p region was high in NCO-20/CC, suggesting the higher adsorption of OH^- on the surface.[Chen et al., 2018] The Ols peak in NCO-20/CC can be deconvoluted into two peaks corresponding to M-O (Co-O or Ni-O) and hydroxyl bond respectively, as seen in Figure 5.12c. The ratio of –OH peak to O ls indicates the extent of hydroxylation, in the following trend NCO-20/CC (0.71), followed by NiO/CC (0.75) < Co_3O_4/CC (0.82) (Table 5.3).

5.4.4 Magnetism Induced OER Measurements

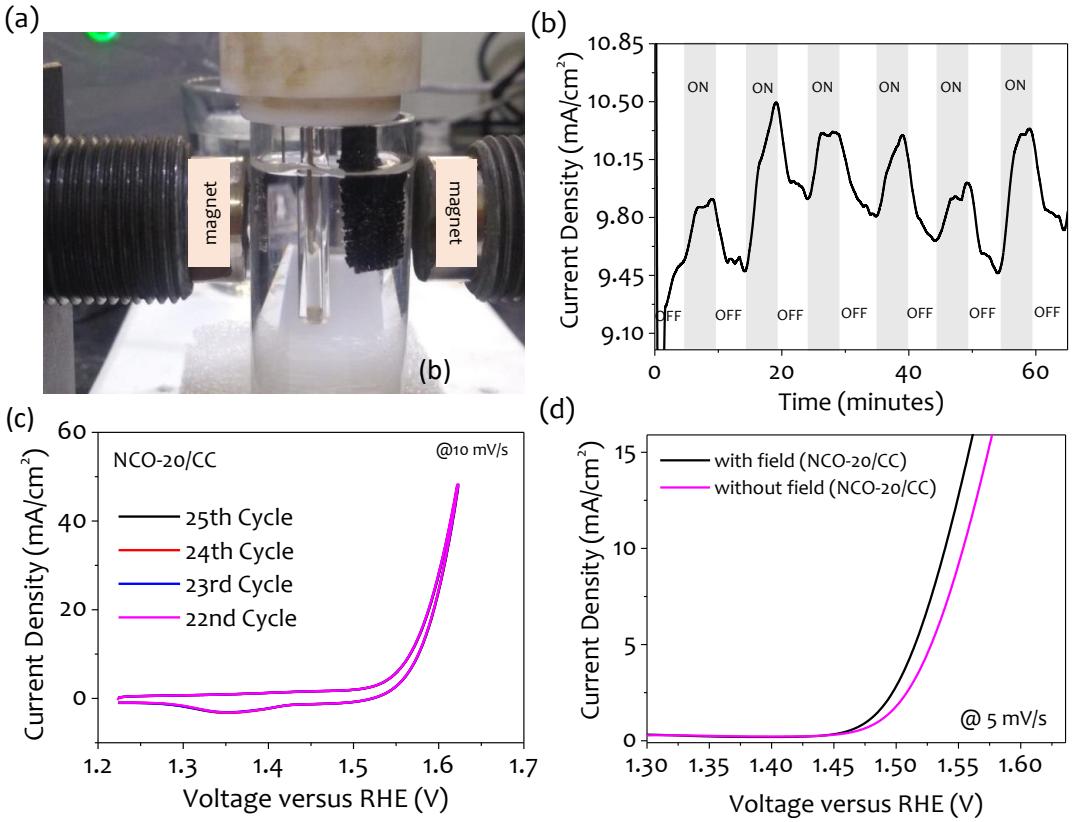

Figure 5.14: (a) Photograph of setup for magnetism induced OER measurements. (b) I-t at overpotential for increment and decrement in the current density with and without a magnetic field of 300 mT. (c) CV curves at 10 mV/s of last 4 consecutive cycles and (d) LSV measurements with and without an applied magnetic field of NCO-20/CC.

Inspired by the superparamagnetic nature (Figure 5.5f) of the NCO at room temperature (300 K), the OER activity of magnetically active NCO-20/CC was analyzed in the presence of a magnetic field (Figure 5.14a and b). The electrodes were activated by CV measurements before carrying out the magnetic field-assisted measurements to obtain a stable response. The overlapping CV curves obtained from last 4 consecutive cycles after electrode activation are shown in Figure 5.14c. The LSV measurements show a reduction in the overpotential by 20 mV on applying magnetic field (Figure 5.14d). A ~5% increase in current density was observed with a magneto current density of 0.5 mA/cm^2 for repeated magnetic field on-off cycles. Since the mass of $NiCo_2O_4$ is low, the increment is small yet appreciable. This change can be explained based on the magnetic hydrodynamic effect (providing stirring-type action) and reduced energy gap between the redox couple in the presence of a magnetic field, thus enhancing the overall OER performance.[Li et al., 2019b]. The magneto hydrodynamic effect is dependent on the magnetic field direction; the Lorentz force reaches a highest value when the magnetic field is perpendicular to the electric field of the active electrode.[Li et al., 2019] Hence, during the experiments, the magnetic field was kept perpendicular to the electric field to obtain the maximum mass transport and increase in current density. When the magnetic field is parallel to the electric field, no change in the OER is observed which is plausible as there is no contribution from the intrinsically spin-polarized intermediates.[Garcés-Pineda et al., 2019; Saha et al., 2021] Thus, the above observations indicate that major effects are from magnetohydrodynamics only. Indeed the effect of the stabilization of spin states on OER activity would be desirous for it may require further design of experiments and detailed optimization of loading of superparamagnetic nanoplates for enhancing the magneto-current density.

In summary, the structural changes due to catalytically advantageous nanoplates of $NiCo_2O_4$ spinel formed in NCO-20/CC are mainly responsible for higher electrical conductivity and enhanced catalytic sites, simultaneously reducing the activation energy necessary for oxygen evolution.[Karakitsou et al., 2005] It is also worth noting that a highly conductive CC substrate as a support system for the $NiCo_2O_4$ spinel structure also plays a vital role in intensifying the OER enhancement. However, despite the novel synthesis method, $NiCo_2O_4$ nanoplate is a well-studied system in the literature. As seen from the literature comparison in Table 1.3, various efforts have been made in the literature reports, including the growth of nanostructures, doping with elements like Mn, Fe, and P, usage of highly conducting metallic backbone, and composites of various oxides in combination with 2D materials for enhancing the $NiCo_2O_4$ performance. These methods involve tedious, time-consuming, and sophisticated techniques for their growth and electrode fabrication. Interestingly, the method developed in this study outstands in terms of easy fabrication, does not require any special treatment, and is easily scalable. Furthermore, it provides the advantage of reduced resistances due to the elimination of additives and binders. This method is economical without compromising the performance parameters like overpotential, Tafel slope, and TOF values as compared with the rest of the literature (Table 1.3). This solution-processable method can utilize the micro-macro-areas, which proffers it an added advantage for the deposition of ink forming NCOs. The CC acts as a 3D substrate that provides multiple sites to NCO nanoparticles for deposition and enables efficient charge transport. The overall performance of electrocatalyst is worth appreciating because even though the mass loading is limited by the dip-coating of the substrate in precursor ink, the OER performance is not sacrificed. Any other conductive 3D backbone of either carbon or metal with a high surface area can be used as a support system for the conformal coating of Ni-Co ink developed in this study.

5.5 Conclusions

In conclusion, we have demonstrated a scalable fabrication technique for $NiCo_2O_4$ nanoplates with single crystallinity supported on CC. The Co:Ni thiolate forms ordered assemblies at an optimized molar ratio (4:1) that on solventless thermolysis results in nanoplates. The Co-Ni oxide coated on CC fibers (NCO-20/CC) act as an efficient electrocatalyst for OER reaction with a low overpotential of 310 mV and Tafel slope of 68.5 mV/dec contrast to pristine oxides due to high electrical conductivity and single crystalline nature leading to highly active reactive sites of Ni^{3+} and Co^{3+} species on the surface. Magnetic measurements show the superparamagnetic behavior in NCO-20 due to the formation of ultra-thin nanoplate of Co-Ni spinel. The superparamagnetic properties are advantageous in improvising the OER performance by enhancing the magneto-current density under the applied magnetic field. Thus, in the present work, a novel method has been described to produce a highly efficient and stable electrocatalyst for OER on a large scale that has potential application in other areas owing to its interesting structure, magnetic and electrochemical properties.